Atmospheric Pollution Research 9 (2018) 901–911

HOSTED BY

Contents lists available at ScienceDirect

Atmospheric Pollution Research

journal homepage: www.elsevier.com/locate/apr

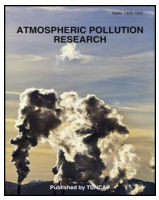

Short-term passive tracer plume dispersion in convective boundary layer using a high-resolution WRF-ARW model

Sudheer R. Bhimireddy, Kiran Bhaganagar*

Laboratory of Turbulence, Sensing and Intelligence Systems, Dept. of Mechanical Engineering, University of Texas, San Antonio, TX, USA

ARTICLE INFO

Keywords:
Scalar plume dispersion
Convective regimes
High-resolution WRF-ARW
Passive tracers
Convective transport

ABSTRACT

High-resolution Advanced Research Weather Research and Forecast model is used to understand the role of atmospheric stability on the short-term transport of a continuous release passive scalar plume in three different convective boundary layer regimes: highly convective, combined shear- and buoyancy and shear dominated. Friction velocity to convective velocity ratio and atmospheric stability parameter are used to classify the boundary layer regimes. The effect of release height on the plume transport is addressed by releasing the plumes at surface, near-surface and elevated heights. Total 144 simulations are performed by releasing the plume in the morning and afternoon times of January and August months and at three release heights. Results show that horizontal transport of the plume scales with the initial wind conditions for surface and near-surface releases, and the vertical transport scales with atmospheric stability parameter. Mean plume height and vertical dispersion parameter obtained by convective scaling laws reached their asymptotic values after getting well-mixed in the boundary layer. The dimensionless downwind distance for the mean plume height to reach its asymptote is found to follow a power-law with respect to the atmospheric stability paramter. The coefficient and exponent of the power-law observed are found to be functions of the plume release height normalized by the boundary layer depth.

1. Introduction

Above the ground, a convective boundary layer (CBL) exists due to the forcing by the buoyancy production at the surface of the earth (heating of the ground) and due to the wind shear. The combined effect of convection- (buoyancy) and mechanical- (shear) generation of turbulence result in layer of well-mixed turbulence in CBL (Turner, 1994). On the release of a plume in a CBL, the relative role of buoyancy and wind-shear play a significant role in the plume transport. This is a very challenging problem, and very little is understood of the effect of plume transport under various realistic conditions of the CBL.

Fundamental studies have contributed significantly to our basic understanding on the key CBL dynamics that influence the plume transport. For CBL the Near-Neutral conditions occur when dominant motions are shear-induced. During moderate and stronger convective conditions, depending on their relative strength, both shear- and buoyancy interact resulting in turbulent longitudinal vortices with updrafts and downdrafts originating near the ground. Thus, creating a vertical flux of momentum, buoyancy and scalars. During these conditions, studies have demonstrated that the plume centerline deviates from its emission height and instead loops up and down (Bierly and Hewson, 1962; Briggs, 1965); and the plume spreads about this centerline (Gifford, 1960; Garratt et al., 1992). When averaged over longer time-periods covering many convective circulations, the plume centerline height vs. downwind distance exhibits stationary pattern (Briggs, 1993; Stull, 2012).

The mixing layer height of the CBL and turbulence in this layer play an important role in dictating the vertical transport of the plume. Pollutants released into shallow boundary layer have limited vertical transport (Banta et al., 2005; Petäjä et al., 2016), when compared to those releases into deeper boundary layers (Banta et al., 1998; Stull, 2012). A shallow CBL e.g. occurs during summer early mornings, with limited mixing height restricts the vertical transport of plume elements (Lyons and Cole, 1973; Stull, 2012). Lyons and Cole (1973) observed large degree of mixing (especially in horizontal) and greater horizontal transport of pollutants when they are released into a shallow mixed layer of 135 m from a 20 m height exhaust stack of a fertilizer plant located in Michigan, United States of America (USA). As the boundary layer deepens during late afternoons, the formation of convective eddies carry the plume elements aloft. Banta et al. (1998) observed

Peer review under responsibility of Turkish National Committee for Air Pollution Research and Control.
* Corresponding author. EB 3.04.16, Dept. of Mechanical Engineering, 1 UTSA Circle, San Antonio, TX, 78249, USA.
E-mail address: kiran.bhaganagar@utsa.edu (K. Bhaganagar).

https://doi.org/10.1016/j.apr.2018.02.010
Received 26 October 2017; Received in revised form 18 February 2018; Accepted 23 February 2018
Available online 10 March 2018

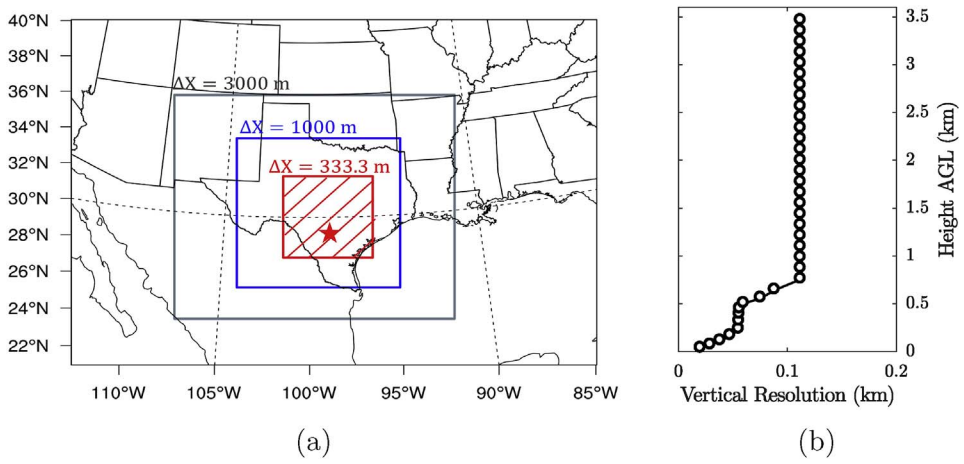

Fig. 1. (a) WRF Model Domain configuration with 3 nested domains. The parent domain has horizontal grid resolution of 12km. Red Star indicates the passive tracer release location. (b) Model vertical resolution as a function of altitude.

reduction in horizontal transport of Ozone elements because of the existence of deep mixing layer and light winds over Nashville, USA. The horizontal transport scales of the pollutant are governed by the wind shear, wind strength and the local atmospheric turbulence (Barr et al., 1983; Banta et al., 1998). It is clear that the interplay of the wind shear, wind strength, buoyancy, and the turbulence together govern the horizontal and vertical transport of the plume. Thus, the study of plume transport is tightly connected to the understanding of the dynamics of the CBL.

The regimes of the CBL are quantified using CBL metrics shear-buoyancy ratio (u_*/w_*) and the stability parameter ($\zeta = -z_i/L$), (where u_* is friction velocity, w_* is convective velocity, z_i is CBL height and L is the Monin-Obukhov length scale) (Dosio et al., 2003). Based on the above CBL metrics, the atmospheric regimes used in this study are as follows: (1) Pure Convective (B) regime which is mainly dominated by buoyancy forcings and is highly unstable with large subsidence ($u_*/w_* \leq 0.2$, $\zeta \geq 40$), (2) Shear-Buoyancy (SB) regime with both shear- and buoyancy forcings, and is moderately unstable ($u_*/w_* \approx 0.3$, $\zeta \cong 10$), and (3) Near-Neutral (NN) CBL regime, which is shear dominated and is weekly unstable ($u_*/w_* \sim 0.6$, $\zeta \sim 2$). The study addresses an outstanding question on differences in the short-term transport of non-buoyant plumes under these different CBL regimes.

Most of our current understanding of short-term transport of passive plumes from laboratory-based experimental measurements (Deardorff, 1985; Willis and Deardorff, 1976, 1978) or high-resolution large-eddy simulations (Nieuwstadt, 1992; Dosio et al., 2003) use idealized conditions. Recent numerical studies of Dosio et al. (2003), and Nottrott et al. (2014) focused on the dispersion of passive scalars released into various convective conditions use quasi-equilibrium state of the CBL as initial conditions, which does not account for the true state of the atmosphere. Towards this direction, significant work was performed recently on using Advanced Research Version of Weather Research and Forecast (WRF-ARW) as a modeling platform to study plume transport (Yerramilli et al., 2009; Yu et al., 2012; Yver et al., 2013; Nottrott et al., 2014; Blaylock et al., 2017). Further, it was established that simulated meteorological data using WRF-ARW model are closer to the observations(Yerramilli et al., 2009; Coniglio et al., 2013; Avolio et al., 2017).

The present work is different from these existing works, as we use high-resolution WRF-ARW v3.8 (hereafter WRF) (Skamarock and Klemp, 2008); with realistic boundary conditions derived from National Center for Environmental Prediction (NCEP) North American Model Analysis (NAM-ANL) dataset. A scalar transport equation included in WRF represents the transport of the passive tracers. The study includes the effect of large-scale atmospheric forcing on the short-term transport of non-buoyant (passive) and conservative (without chemical reactions or chemical mixing) tracer plumes in different CBL regimes. The objective of the study is to address the question - what is the effect of the atmospheric stability and release height on the dispersion of passive plumes when released in different CBL regimes.

As the input data for WRF model is available at coarser resolution, the initial and boundary conditions to actual domain are obtained by multiple nested WRF domains. The regional domain for all the cases is the Bexar County located in the south-central part of Texas, United States. Passive tracers are initialized in the center of the county (29.4241^o N, 98.4936^o W), which is the downtown area of the City of San Antonio. Before emitting the passive tracers into atmosphere, the WRF model is spun-up for 12 h. The release times are 0700 CST (= UTC-6 hours) and 1300 CST during the months of January and August. For studying the effect of different release heights (z_s), the passive tracers are released at surface level ($z_s/z_i = 0$), near surface level ($z_s/z_i < 0.1$) and far from surface ($z_s/z_i > 0.1$). In this study, cases are simulated for 12 days in each of January and August months with a total of 144 realizations. Post-processed variables are ensemble averaged over their 12 realizations. The individual realizations selected have their wind-speed and temperature deviations of order 1–2 m/sec and 2–5 K from the respective ensemble mean values.

The structure of this paper is as follows: Section 2 summarizes the methodology followed using WRF for configuring the simulations. Section 3 explains different case studies simulated in the study. Section 4 gives the WRF model validation with the observed values from meteorological stations and a chosen field experiment data to validate the tracer transport. Tracer transport results in both horizontal and vertical are presented in Section 5. Detailed analysis of tracer vertical transport using convective scaling laws is presented in Section 6.

2. Methodology

2.1. Domain configuration

The WRF model is configured with four nested domains with the outer domain having the same resolution of 12 km as the data-set used for boundary conditions. Remaining three nested domains are at horizontal resolutions of 3 km, 1 km and 333.33 m in the inner most domain, which is shown in Fig. 1 (a). 38 vertical levels are configured between the surface and 3500 m, with 14 levels located in the lowest 1000 m above the surface, shown in Fig. 1(b). The first model level top is specified at an altitude of 20.8 m above the surface. The initial and lateral boundary conditions needed for WRF are provided by the meteorological datasets obtained from the NAM-ANL dataset over the grid 218 with a spatial resolution of 12 km, 40 vertical levels and 4 samples per day. Run by NCEP, NAM-ANL is one of their major weather forecast models and it is initialized with a 6-hour data assimilation cycle with

Table 1
WRF model configuration.

WRF Model Physics	
Longwave Radiation	RRTM scheme (Mlawer et al., 1997)
Shortwave Radiation	MM5 scheme (Dudhia, 1989)
Microphysics	Ferrier (Ferrier et al., 2002)
Cumulus	Kain-Fritsch (Kain and Fritsch, 1993)
PBL	YSU scheme with ysutopdownmixing turned "on" (Hong et al., 2006; Hu et al., 2010; Noh et al., 2003)
Surface layer	Monin-Obukhov (Janjic, 1996)
Land Surface model	Noah LSM (Ek et al., 2003)

hourly analysis updates.

The horizontal turbulence and mixing is computed using 2^{nd} order horizontal diffusion on model levels, while the vertical mixing is evaluated from the Planetary boundary layer (PBL) scheme. The eddy coefficient, K, is computed using $2D$ Smagorinsky first order closure method. The scalar mixing and the PBL tracer mixing options in WRF are turned on so that the turbulence parameterized by the PBL scheme is used to mix the passive tracers. The model physics chosen in WRF are outlined in Table 1.

The plume is introduced as passive tracers released from a WRF grid cell. In WRF environment, passive tracers have no physical properties to react with atmospheric compounds and have no influence on the environmental parameters. They are transported by the models predicted wind and turbulent transport provided by the PBL schemes. Passive tracers in WRF are subjected to same forcing as that of scalars variables present in the model (like water vapor mixing ratio, cloud vapor etc.). To have a continuous release, passive tracers in the present study are emitted into the atmosphere at every time step of the simulation. The WRF source code is modified to allow tracers to be released from any chosen location inside the model domain and after the spin-up period.

3. Case configurations

The Pasquill stability classes during the simulation runs are obtained from Golder's relations (Golder, 1972) using L^{-1} and roughness length (z_o) of the model domain. The nomenclature followed for identifying the cases and their respective Pasquill stability class at the release time is given in Table 2. Initial conditions of friction velocity to convective velocity ratio (u_*/w_*), stability parameter ζ and dimensionless release heights (z_s/z_i) given in Table 2 are ensemble averages of the 12 individual realizations.

Vertical profiles of ensemble averaged mean horizontal $\overline{U}$ (m/sec) and vertical wind speeds $\overline{W}$ (m/sec) are shown in Fig. 2(a) and (b). WRF model simulated geostrophic winds $\overline{U_g}$ (m/sec) for NN regimes are strongest with a magnitude of 11 m/sec and weakest for B regime with 3 m/sec. $\overline{U_g}$ for SB1 and SB2 regimes are in between the NN regime and B regime with magnitudes of 4.5 m/sec and 6 m/sec respectively. The effect of dominant winds during NN regime on plumes horizontal transport are discussed later in detail in Section 5.1.1.

Table 2
Classification of convective boundary layer and initial conditions for different cases simulated in WRF.

Case ID	Pasquill Class	Type of CBL	u_*/w_*	ζ	z_s/z_i
1	C	Near-Neutral(NN)	0.6	1.12	0
2	C	Near-Neutral	0.6	1.12	0.09
3	C	Near-Neutral	0.6	1.12	0.65
4	B	Shear-Buoyancy(SB1)	0.3	10.3	0
5	B	Shear-Buoyancy	0.3	10.3	0.04
6	B	Shear-Buoyancy	0.3	10.3	0.25
7	B	Shear-Buoyancy(SB2)	0.37	7.2	0
8	B	Shear-Buoyancy	0.37	7.2	0.07
9	B	Shear-Buoyancy	0.37	7.2	0.43
10	A	Pure Convection (B)	0.1	152.4	0
11	A	Pure Convection	0.1	152.4	0.02
12	A	Pure Convection	0.1	152.4	0.12

As pointed out by Moeng and Sullivan (1994), mean wind profile during pure convective regime is well-mixed. Whereas for near-neutral regimes, a strong mean vertical gradient is present. From ensemble mean wind profiles, NN regime with highest shear and B regime with least or negligible shear acts as two extremes within convective atmosphere with SB regimes shear falling between these two. Under NN regime, most of the turbulence is mechanically generated due to the presence of shear (Turner, 1994). For SB1-SB2 regime, this turbulence is generated by both shear and buoyant forcing, while for B regime mixing happens primarily due to buoyant generation of turbulence (Sykes and Henn, 1989; Moeng and Sullivan, 1994). For buoyancy dominated flows, in B regime, horizontally averaged mean vertical velocity profile shows presence of strong updrafts with maximum observed near to 0.5 z_i. This behavior is not observed for NN and SB1 regimes. In SB2 regime, positive values of domain averaged mean vertical wind are present with maximum occurring near to surface. This is expected during the morning times when updrafts are getting stronger than downdrafts because of increasing buoyancy near the surface (Stull, 2012). Non-zero values of $\overline{W}$ were also observed during CONDORS (CONvective Diffusion Observed with Remote Sensing) field experiment, during which the 40-min averaged values of $\overline{W}$ were recorded as high as +30 cm/sec (Period 35, 38 cases in Briggs (1993)). $\overline{W}$ measurements during the CONDORS experiment were collected from a single 300 m meteorological tower at Boulder Atmospheric Observatory (BAO) located close to the release location. $\overline{W}$ evaluated at the source location of present study have similar profile (not shown) with maximum occurring close to $0.5z_i$. Venkatram (1984) in his model for evaluating the effect of nonzero $\overline{W}$ on CBL dispersion, estimated $\overline{W}^2$ to be $3\sigma_w^2 z_i/t_s \overline{U}$, where σ_w being the standard deviation of vertical velocity and t_s is the averaging time in seconds. For $\sigma_w \approx 0.6w_*$, the 4-hour averaged values of $\overline{W}/w_*$ near release location of our study are found to be 0.2; which is very close to the values observed during Period 35 (0.18) and 38 (0.22) of CONDORS experiment (Briggs, 1993).

The shear and buoyancy tendencies within the cases simulated are expressed in terms of wind shear exponent (α) and Bulk-Richardson number (Ri_B). Shear exponent α is defined using power law as:

$$\alpha = \frac{log\,(\overline{U}_z/\overline{U}_{z_{Ref}})}{log\,(z/z_{Ref})} \tag{1}$$

where, $\overline{U}_z$ is the mean wind speed as a function of height and time, z_{Ref} is the reference altitude. Fig. 3 gives the 4-hour time and domain averaged $\langle\alpha\rangle$ and $\langle Ri_B\rangle$ with respect to the stability parameter ζ. The overall variation of $\langle\alpha\rangle$ and $\langle Ri_B\rangle$ during the simulation runs are within their respective CBL classifications, meaning that the CBL regime has not changed during the averaging times of 4-hours. Similar $\langle\alpha\rangle$ values are observed by Smith et al. (2002); Schwartz and Elliott (2006) during winter and summer months at Ft.Davis and Sweetwater areas in Texas. Vanderwende and Lundquist (2012) observed similar convective conditions in Central North America based on the shear-exponent and Bulk-Richardson number values.

4. WRF model validation

4.1. Meteorological variables validation

The WRF simulated hourly meteorological variables of 10 m wind speed, direction and 2 m temperature are compared against the averaged values obtained from nearby 5 Continuous Ambient Monitoring Stations (CAMS) that are operated by Texas Commission on Environmental Quality (TCEQ, 2017). Locations of the stations considered and their radial distance from the source are given in Table 3.

The WRF simulated 10 m wind speed, direction and 2 m temperature fields are averaged over the innermost domain for all the simulations

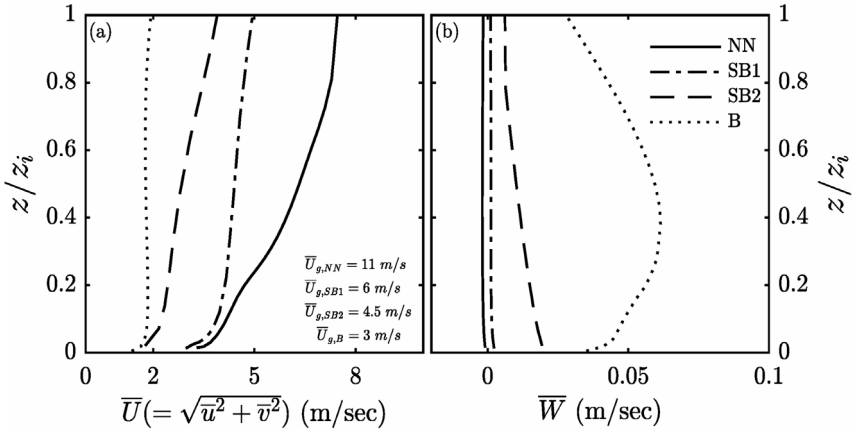

Fig. 2. Vertical Profiles of mean horizontal wind speed and mean vertical velocity for (a) NN, (b) SB1, (c) SB2, (d) B cases simulated.

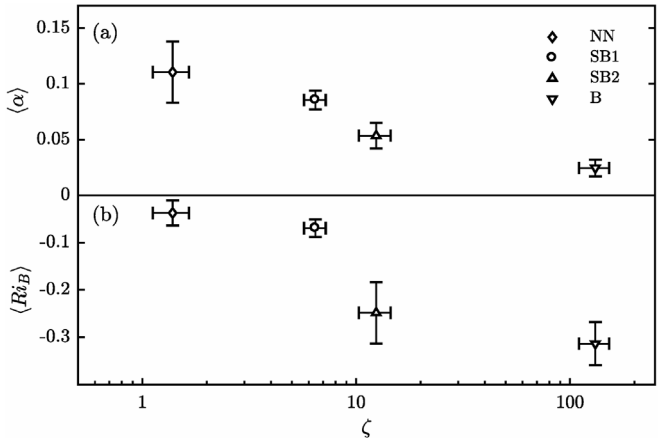

Fig. 3. Time averaged (a) ensemble Wind shear exponent, (b) ensemble Bulk-Richardson number averaged over the entire CBL of innermost model domain with respect to stability parameter. The whiskers in (a) and (b) represent the range of variations during the averaged period.

Table 3
Details of meteorological stations from which 10 *m* wind speed, direction and 2 *m* temperature are obtained. Radial distance reported is with respect to the source location.

Station ID	Latitude (°N)	Longitude (°W)	Radial Distance (*km*)
CAMS 0023	29.51509	−98.62017	16
CAMS 0058	29.63205	−98.56494	24
CAMS 0059	29.27538	−98.31169	24
CAMS 0677	29.42394	−98.58049	8
CAMS 1069	29.52940	−98.39139	15

Table 4
Comparison between WRF simulated and observed wind speed, wind direction and temperature data.

Regime	Bias			STDE		
	$\overline{U}$ (*m/sec*)	$\overline{U}_{Dir}$ (°)	$\overline{T}$ (*K*)	$\overline{U}$ (*m/sec*)	$\overline{U}_{Dir}$ (°)	$\overline{T}$ (*K*)
NN	0.27	3.19	1.49	0.37	17.19	3.50
SB1	0.15	2.87	0.89	0.45	20.91	3.27
SB2	0.18	−3.72	−0.77	0.33	29.26	2.82
B	0.08	2.46	0.29	0.17	18.86	1.37

performed and respective observed values are obtained from the stations. The statistical measures of Bias and Standard Deviation of the Error (STDE) as defined in Carvalho et al. (2014) are used to evaluate the WRF simulated meteorological fields and are given in Table 4. A positive bias shows that the WRF model overestimated the values, while a negative bias indicates underestimation by WRF. In case of wind direction, a positive value indicates WRF simulated wind are deviated in clockwise direction and a negative value indicates their deviation in counter-clockwise direction. Except for wind direction and temperature in SB2 regime, WRF model overestimated the meteorological fields for rest of the regimes. Simulations in B regime has the lowest bias and STDE for all the three variables compared. Simulations in NN regime has the highest bias from the observed values.

Overall, better agreement is found between WRF simulated wind speed and temperature with observed values during highly convective conditions.

4.2. Tracer transport validation

In the present study, the tracer transport with the chosen WRF physics and dynamics options is validated against Oklahoma City field experiment campaign (OKC-80) (Ferber et al., 1981). Data from Data Archive of Tracer Experiments and Meteorology (DATEM) is used for this purpose. The OKC-80 experiment consisted of non-buoyant tracer release during July 08 and July 09 of 1980. Later, air samples were collected at 10 sites along 100 *km* arc downwind from the Oklahoma City release point (Ferber et al., 1981). WRF preprocessing system was configured to the experiment location and all the options were kept same as described earlier in the model configuration. In the WRF model, tracers were simulated using WRF inbuilt passive tracers initialized with source strength of 186000 *units* and were released at surface level from 1900 GMT (= CST + 5 h) to 2200 GMT on July 08. The model was spin-up for 12 h before the tracers were released.

The sampling sites are selected based on their proximity to the grid points in the WRF model domain. The tracer transport results are compared against the concentration readings obtained from the surface sampling sites # 12,13,14,15,16,18,19,20. Samples during the experiment were collected for 45 min and the 45-minute time averaged concentrations were reported (Ferber et al., 1981). The tracer concentrations measured in parts per 10^{15} from the OKC dataset and the WRF simulated data from 2100 GMT on July 08 to 0000 GMT on July 09 are as shown in Fig. 4. WRF simulated concentrations are slightly underestimated with R^2 value of 0.962. With a root-mean square error of 366 parts per 10^{15} between the simulated and observed concentrations, the current methodology is considered satisfactory enough to simulate short-range transport of passive tracers.

5. Transport scales of passive tracers in horizontal and vertical

The ensemble-averaged results over the 12 realizations for each source height and stability conditions are presented below. Plume

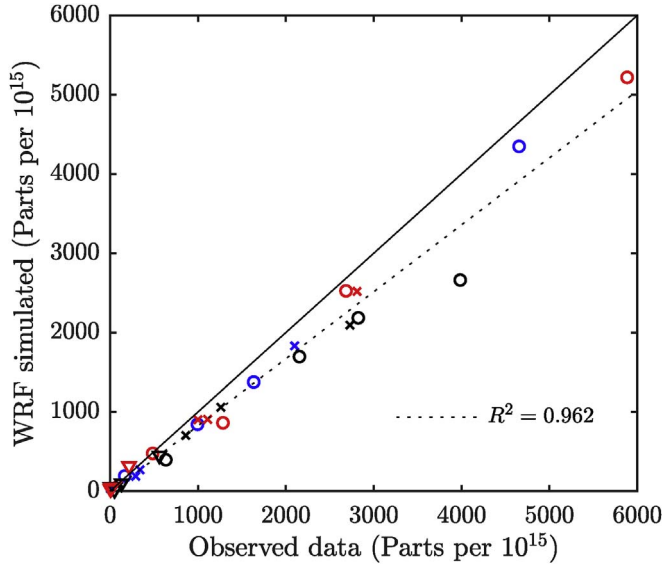

Fig. 4. WRF modeled and Observed data during 2100 *GMT July*08 to 0000 *GMT July* 09 along sampling sites #12 (black circles), #13 (red circles), #14 (blue circles), #15 (black cross), #16 (red cross), #18 (blue cross), #19 (black inverted triangle), #20 (red inverted triangle) in OKC experiment.

transport analysis is done in two parts; first the horizontal transport of the plume elements is discussed in detail and later the vertical transport and dispersion in the CBL are discussed.

5.1. Horizontal transport

Transport of pollutants within CBL is dominated in horizontal direction by mean wind and in vertical direction by convective forcing (Stull, 2012). During winter morning releases, the atmospheric conditions simulated are weakly convective (near neutral) with the presence of strong wind-shear as seen from both vertical profile of mean wind (Fig. 2(a)) and wind shear exponent (Fig. 3(a)). Fig. 5 shows the ensemble horizontal transport scales of the passive tracer plume during first four hours after the release for all the cases simulated. The horizontal distance travelled by the plume is evaluated as the distance from the source location to the plume front along plume downwind direction. For the NN regime, presence of strong winds and weak buoyant forcing transported the passive tracers to larger distances, approximately 60 *km* from source location in 4 h. During the pure convection regimes, the horizontal advection of the passive tracers is observed to be minimum, approx. 20 *km* in 4 h. For shear-buoyancy regime (SB1-SB2), with moderate wind speeds and buoyant forcing in CBL, the passive tracers are advected to around 40–50 *km* in 4 h from release.

For prediction analysis, a horizontal length scale ($\overline{S}_{predicted}$) based on the mean wind-speed is formulated to predict the transport scales of the tracer plumes using the initial meteorological wind conditions. The length scale

$$\overline{S}_{predicted} = \begin{cases} \overline{U}_0(z_s)t, & \text{for } t < 30min \\ \overline{U}_0(z_{i/2})t, & \text{otherwise} \end{cases} \quad (2)$$

is based on the initial mean wind-speed at the release altitude ($\overline{U}_0(z_s)$) for first 30-minutes after the release, and for later times based on the wind-speed at the half-height of CBL, i.e. at $z_i/2$. The 30-minute threshold considered is based on the literature that plume elements will be uniformly mixed within CBL by that time because of convective turbulence in the mixed layer (Willis and Deardorff, 1976, 1978; Weil et al., 2012; Stull, 2012). For surface releases, mean wind from the nearest vertical grid-point is considered for the initial 30-minute period. The horizontal transport scales predicted from initial wind profile ($\overline{S}_{predicted}$) are compared against the WRF simulated ones ($\overline{S}_{WRF}$) (Fig. 5).

For comparison, maximum error (ε_{max}) and normalized root-mean square error (RMSE) defined by

$$\varepsilon_{max} = max(\overline{S}_{predicted} - \overline{S}_{WRF})$$
$$RMSE = \frac{\sqrt{\Sigma(\overline{S}_{predicted} - \overline{S}_{WRF})^2 / n}}{max(\overline{S}_{WRF})} \quad (3)$$

are evaluated.

During NN regime, the horizontal transport using $\overline{U}_0$ is under-predicted than WRF transport. This is observed for all the release heights in NN regime (Fig. 5(a, b) and (c)). Moreover, the maximum error observed during NN regime is during the first 30-minutes after release for surface ($\varepsilon_{max} = -8.01km$) and near-surface releases ($\varepsilon_{max} = -8.9km$). For elevated releases ($z_s/z_i = 0.65$) during NN regime, the maximum error ($\varepsilon_{max} = -11.54km$) is observed towards the end of 4-hour period.

For short-term prediction of the plume transport, it is important to justify the efficacy in using the conditions at the release time for scaling. Consistent with ε_{max}, the RMSE for NN regime increases with increase in release height. Even though the ε_{max} evaluated for surface release case during B regime is the least among all the cases shown in Fig. 5, it's RMSE is 0.08 which is closer to the RMSE evaluated for surface releases during other CBL regimes. Similarly the RMSE values for near-surface cases are of same magnitude for all the CBL regimes. This suggests that use of initial wind profile for transport prediction is robust enough within 87–93% accuracy for surface and near-surface releases. For elevated releases, significant differences between the predicted scale and simulated transport are found as the maximum error and maximum RMSE are observed. In summary, horizontal transport scales with mean wind speed for surface and near-surface releases, while it deviates for elevated releases. Also, as the normalized RMSE is of same order for NN, SB and B regimes; $\overline{S}_{predicted}$ is more sensitive to release height than the CBL regime.

5.1.1. Visualization of horizontal transport

For visualizing the horizontal transport scales of the passive tracers, column-averaged tracer concentrations are calculated in the inner-most domain and are presented over Google Maps location of the simulated domain. Fig. 6 shows threshold contours (5% of source strength) of column-averaged ensemble of passive tracers in the domain for all the cases after 4-hours from release. For elevated releases ($z_s/z_i > 0.1$), the horizontal advection of the passive tracers is slightly larger than that of near-surface- ($z_s/z_i < 0.1$) and surface- ($z_s/z_i = 0$) releases for all the cases (Fig. 5). This is observed to be true for column averaged concentrations as well (Fig. 6(a)-(d)), where the area covered by 5% threshold contours is large for elevated releases (blue lines).

The effect of the wind direction on the local plume transport is analyzed next. Local wind-rose diagram obtained from the nearby meteorological stations has been plotted against the wind-rose drawn using WRF simulated winds in Fig. 6 during the simulated days of winter (NN and SB1 regimes) and summer months (SB2 and B regimes). The results identify the difference between actual wind direction and mean transport direction calculated from WRF. It is clear that plume transports follows the wind-direction. Strong winds from North-East and East-North-East during NN regime transport the plume elements down West-South-West path as seen in Fig. 6(a). Similarly, During SB1 regime (Fig. 6(b)), winds blowing from South-South-West advect the tracer elements against the wind in the North-North-East direction. However, when the wind direction changes rapidly as in the case of SB2 regime, then a sporadic distribution of tracer elements is observed (Fig. 6(c)). For SB2 regime, stronger winds are observed to blow from West, West-North-West, North-North-West and North directions. For B regime, moderate winds coming from North-West and North directions exist and accordingly the tracer elements are transported towards South and South-East directions of domain (Fig. 6(d)). During winter months (Fig. 6(a) and (b)), the frequency of strong winds ($\overline{U} > 3.5$ *m/sec*) is more when compared to summer months (Fig. 6(c) and (d)). For

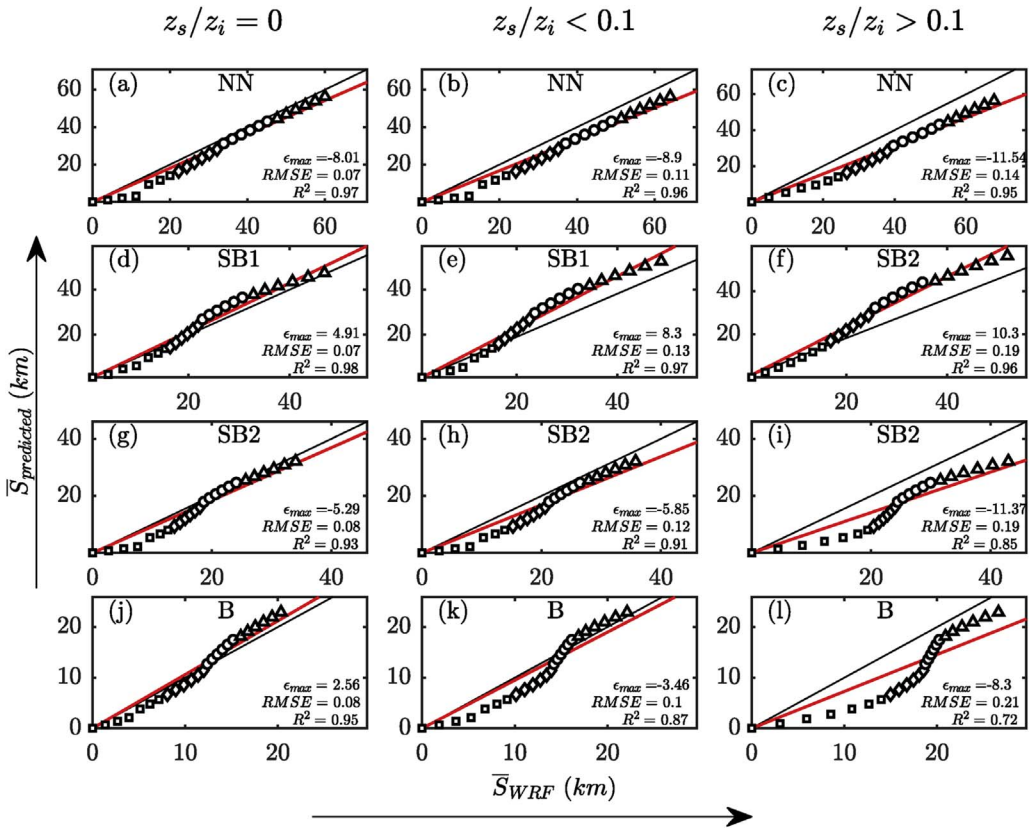

Fig. 5. Ensemble average of the Horizontal distances travelled by passive tracer plumes for cases considered. The linear fit between $\overline{S}_{predicted}$ and $\overline{S}_{WRF}$ is represented by red line and the correlation factor R^2. Horizontal distances travelled during 1^{st}-hour after release are represented by squares, 2^{nd}-hour by diamonds, 3^{rd}-hour by circles and 4^{th}-hour by triangles. (a),(d),(g), (j) are surface releases. (b),(e),(h),(k) are near-surface releases. (c),(f),(i),(l) are elevated releases. (a),(b),(c) are NN regime cases. (d),(e),(f) are SB1 regime cases. (g),(h),(i) are SB2 regime cases. (j),(k),(l) are B regime cases. Cases (a)–(f) corresponds to winter and (g)–(l) corresponds to summer.

elevated releases during pure convection regimes, the threshold contour reached greater distances than the near-surface and surface-releases as shown in Fig. 6(d).

The ensemble transport of the passive tracers in WRF is in good agreement with the mean wind direction over the domain area for winter months. Thus, suggesting that the wind-direction is an important metric in determining the direction of plume transport during the winter month releases. Whereas, this is not the case for summer month releases, where the plume transport does not correlate well with the wind-direction.

5.2. Vertical transport

Fig. 7 shows the ensemble average of cross-plume concentrations in each convective regime for three release heights simulated. As seen in Fig. 7(a), for the NN regime, high concentration regions are advected close to the release altitude. Whereas, because of convective turbulence as in Fig. 7(b)-(d) pockets of high concentrations are well-mixed near downwind distance within CBL.

As seen from the laboratory experiments of (Willis and Deardorff, 1976, 1978), for elevated releases, a tongue of maximum concentration descends toward the surface (Fig. 7(b)-(d)) as downdrafts comprise a larger area than updrafts (Willis and Deardorff, 1976). In the absence of turbulent motions such as convective eddies or updrafts, plume transport is dominated by the mean wind (see Fig. 7(a)). During strong unstable atmospheric conditions, a combination of weak winds and strong vertical motions in form of thermals rapidly mix the plume elements, as they are slowly advected downwind. With the meteorological conditions like that of B regime in current study, Bhaganagar and Bhimireddy (2017) observed such behavior from passive element transport simulated during convective conditions of chemical plume attack in Syria on April 4, 2017. Trapping of tracer elements by PBL top is observed and is visible from Fig. 7(b) and (d). However, some plume elements are overshot across PBL top due to entrainment for all the cases simulated in the study. This overshoot is strong during pure convection times and is minimum for near-neutral conditions as observed from the tracer profiles shown in Fig. 7.

6. Convective mixed-layer scaling

Next, the plume centerline position and vertical dispersion parameter along its downwind are evaluated for the cross-plume ensembles, and convective scaling laws proposed by Deardorff (1970, 1985) are used to convert them into non-dimensional form.

Convective scaling theory (Deardorff, 1970) based on the convective velocity scale (w_*) is used to scale the vertical transport. The tracer downwind distance x is non-dimensionalized using convective velocity scale, PBL height and mean wind speed as:

$$X = \frac{w_*}{z_i}\frac{x}{\overline{U}} = \frac{w_*}{z_i}t \tag{4}$$

where, $t = x/\overline{U}$ is the travel time of the tracers by Taylors translation hypothesis. The use of X is limited for $\zeta \geq 10$, so for cases where $\zeta < 10$ (NN and SB2 cases) a modified non-dimensional downwind distance X_m is used by substituting the convective velocity scale with a modified velocity scale. Moeng and Sullivan (1994) proposed this modified velocity scale as $w_m^3 = w_*^3 + 5u_*^3$, which relates the convective and friction velocities.The vertical dispersion parameter σ_z of the plume relative to the source height is calculated as per Nieuwstadt (1992) as:

$$\sigma_z^2 = \frac{\int c(z - z_s)^2 dV}{\int c dV} \tag{5}$$

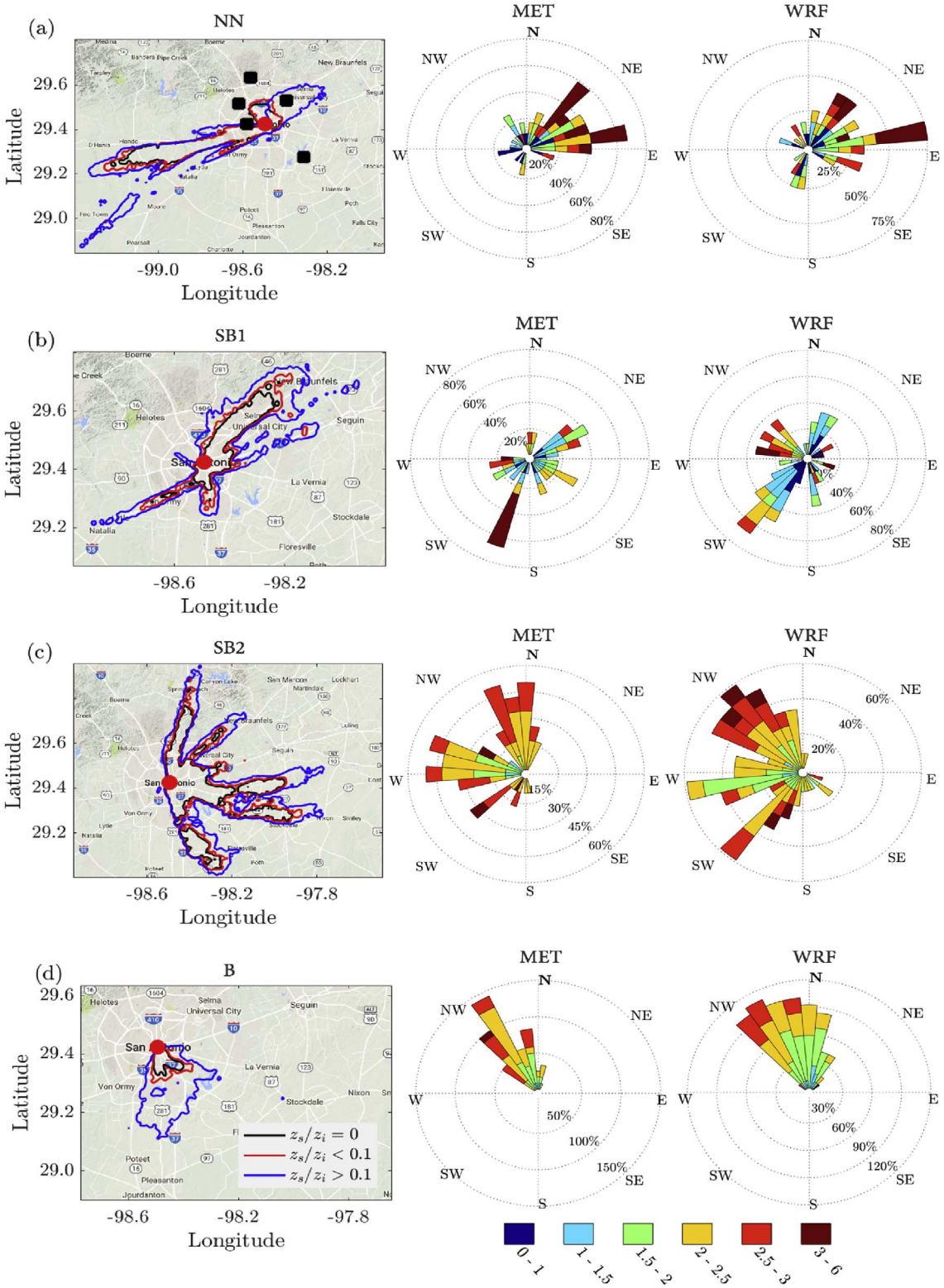

Fig. 6. (left) Vertical average ensemble tracer 5% contours at the end of 4-hours after release for (a) NN, (b) SB1, (c) SB2, (d) B. Red circle represents the source location. (center) Wind Rose diagrams drawn using observed winds from MET stations shown as black squares in 6(a). (right) Wind Rose diagrams drawn using simulated winds from WRF. The color scales for all the contours and wind roses are given in 6(d). Subplots 6(a), 6(b) represents winter transport and 6(c), 6(d) represents summer transport.

where, $dV = dx \times dy \times dz$, z_s is the source release height.

The mean plume height or plume centerline $\overline{z}$ is defined by:

$$\overline{z} = \frac{\int czdV}{\int cdV} \tag{6}$$

The non-dimensional mean plume height ($\overline{z}/z_i$) and vertical dispersion parameter (σ_z/z_i) growth against the dimensionless downwind distances of $X \leq 10$ for all cases are shown in Fig. 8. The dimensionless downwind distance $X \leq 10$ corresponds to roughly 13 km during pure-convection to 35 km for near-neutral cases in 80–100 min from release.

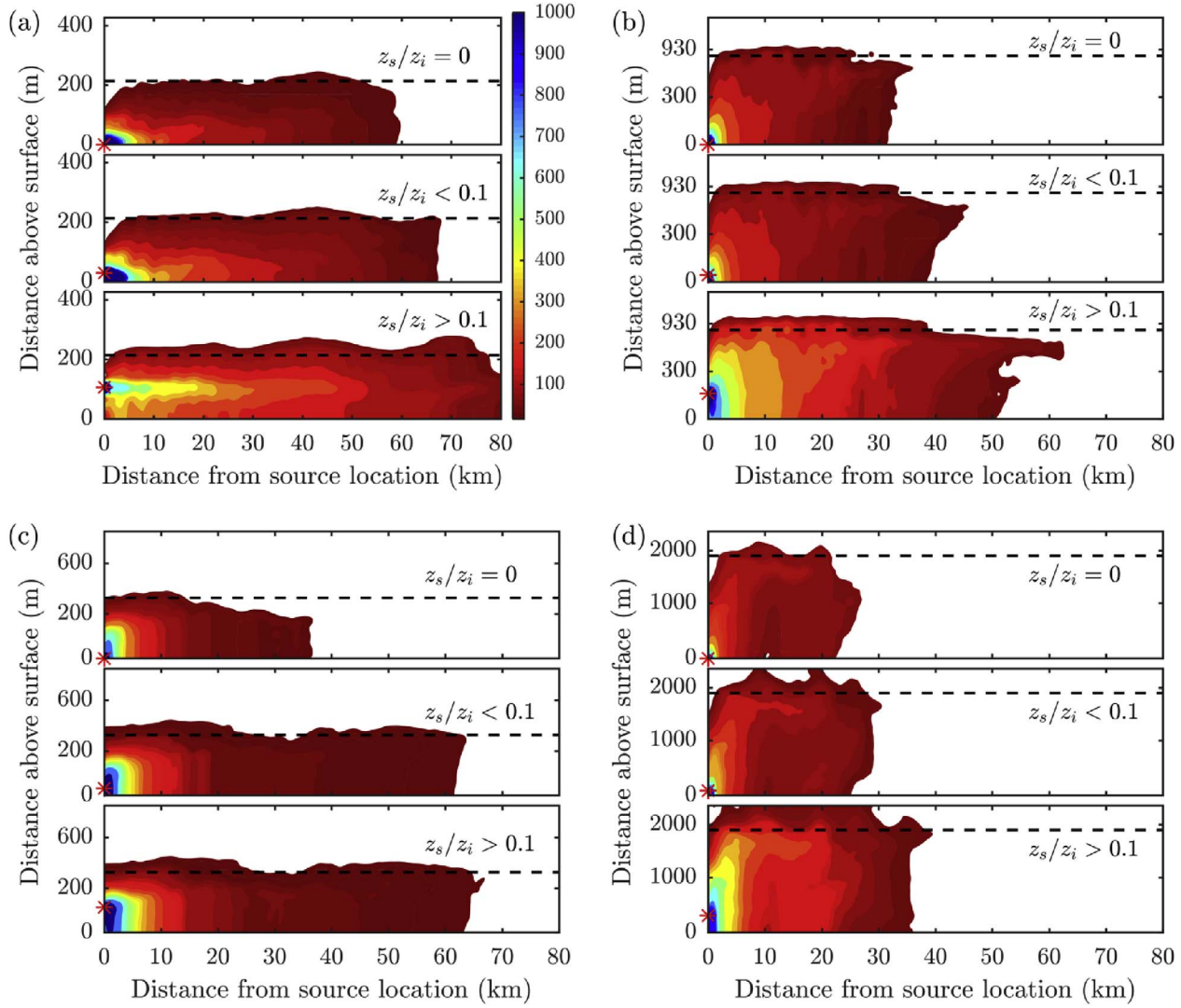

Fig. 7. Ensemble averages of cross-plume concentrations for (a) NN, (b) SB1, (c) SB2 and (d) B cases. Black dashed line represents the PBL top. Red star on the ordinate represents the source location. Color bar representing the passive tracer concentrations for (a)–(d) is given in 7(a).

Once the plume elements are well-mixed within CBL, the time averaged mean plume height reaches an asymptotic value of $0.5z_i$.

The time taken for $\overline{z}$ and σ_z to reach their asymptote values differ based on the regimes of convection as seen from Fig. 8. For cases in NN regime, where the convective turbulence is small, plume elements are slowly mixed within CBL making $\overline{z}$ to reach its asymptote at farther downwind distance of $X_m \approx 4$ (Fig. 8(a)). This is in accordance with the 30-minute criteria used for horizontal transport prediction in Section 5.1. For SB1 and SB2 cases, presence of weak turbulence and shear mixes plume elements more rapidly bringing $\overline{z}$ to its asymptote at nearly $X \approx 3$ (Fig. 8(b)-(c)). For pure-convection cases, presence of strong updrafts and eddies mixes plume elements very quickly, thus mean plume height of $0.5z_i$ is observed at $X \approx 2.5$ (Fig. 8(d)).

The mean plume height for elevated releases during near-neutral conditions is observed to stay near the release altitude, as the vertical forcing due to convective turbulence is not significantly strong to influence the mean plume position. On the other hand, for elevated releases during SB2 case, the mean plume height is observed to dip before it reaches its asymptote limit.

The asymptote value reached by the vertical spread is around $0.4 - 0.45$ for near-neutral cases and it is $0.5 - 0.55$ for others. For ground level releases, presence of impermeable surface restricts the growth of vertical spread close to the source. This is observed for all the ground level cases simulated except for the pure convection case, where the vertical spread growth is much faster than the others. Close to the source location, i.e. for $X_m < 1$ ($x < 2.5$ km), the growth of vertical spread for surface level releases is observed to be linear with a slope of 0.3 for N-N cases, it is linear up to $X_m < 0.8$ ($x < 1.8$ km) with a slope of 0.33 for SB1 cases, and it is linear up to $X_m < 0.65$ ($x < 0.9$ km) with a slope of 0.36 for SB2 cases. As buoyant forcing in the atmosphere increases, the growth rate of vertical spread close to the source location is observed to be increasing resulting in vertical distribution of high concentrations close to surface. For the elevated releases, vertical spread is more than the near-surface releases as the plume elements are influenced by both downdrafts and updrafts. Mean plume characteristics like mean plume height, vertical dispersion parameter are in good agreement with results from Dosio et al. (2003) and Nottrott et al. (2014).

The dimensionless downwind distance X_a, at which the plume elements are uniformly mixed with CBL differs with strength of convective regime. Fig. 9 gives the relation between the stability parameter and downwind distance at which the mean plume height reached its asymptote for all the realization runs. The vertical dotted lines in Fig. 9 represents the breakdown between three convective regimes considered in this study. Realizations with same release height criteria are fitted with power-law of the form:

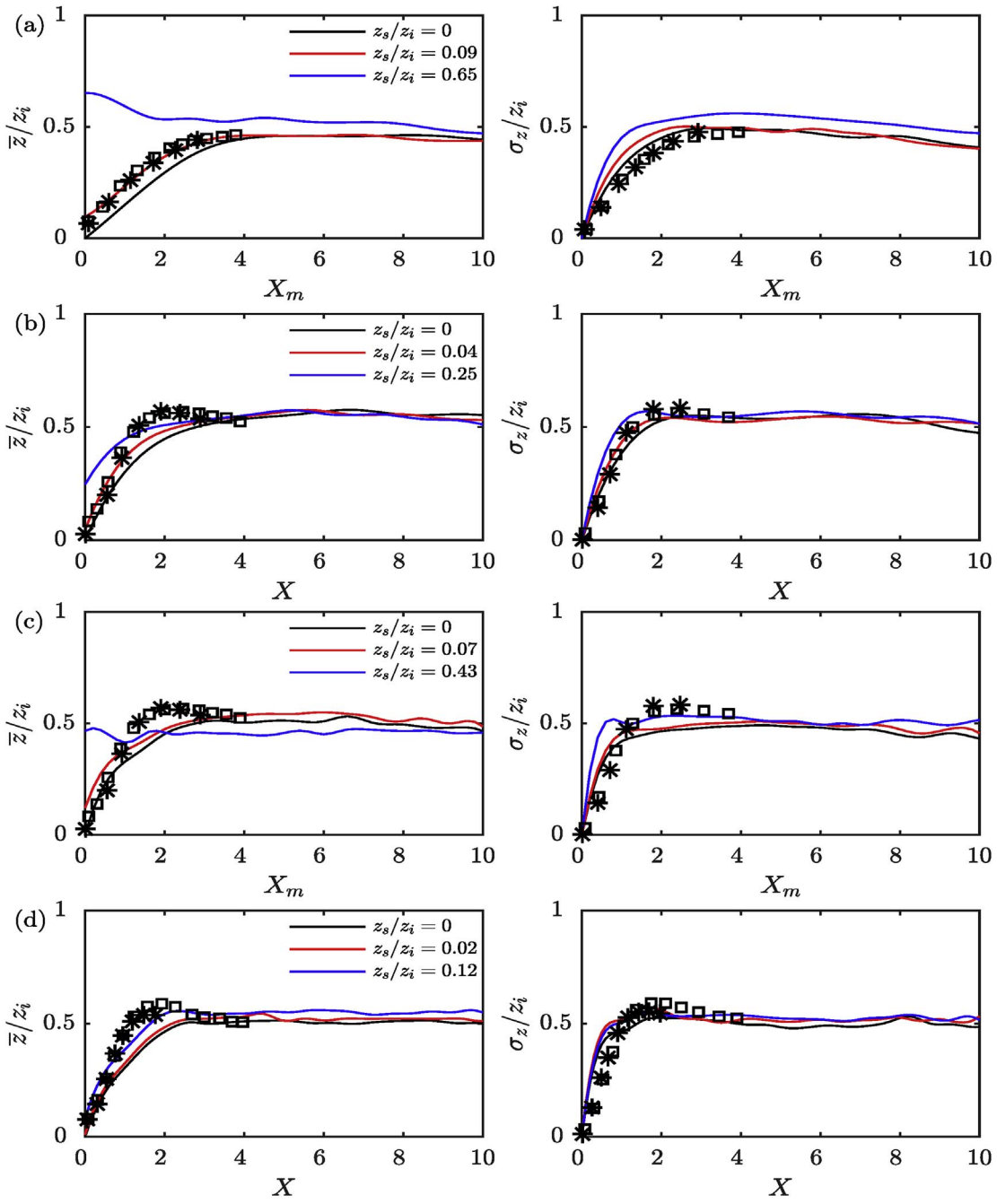

Fig. 8. Mean plume height (left) and vertical dispersion parameter (right) as a function of non-dimensional downwind distance for (a) NN, (b) SB1, (c) SB2, (d) B cases. The black squares represent near surface release LES results of Dosio et al. (2003) and asterisk represents LES results of Nottrott et al. (2014).

$$X_a = A\zeta^B \tag{7}$$

For elevated releases, the plume elements are uniformly distributed close to the source making mean plume height to reach its asymptote at smaller downwind distances. The best fits for realizations at same release heights are given in equation (8). The negative slope of the best-fit indicates that the asymptote downwind distance decreases with increase in buoyant forcing.

As seen in Fig. 8, downwind distance at which the mean plume height reaches an asymptotic value for NN regime releases depend on the release height. The effect of the release height on this asymptotic value reduces as the CBL becomes strongly convective. The best-fit for elevated releases is steeper than the ground release runs (Fig. 9 and Equation (8)).

$$X_a = \begin{cases} 3.98\zeta^{-0.106}, & \text{for } z_s/z_i = 0 \\ 3.25\zeta^{-0.080}, & \text{for } 0 < z_s/z_i < 0.1 \\ 2.66\zeta^{-0.062}, & \text{for } z_s/z_i > 0.1 \end{cases} \tag{8}$$

The power-law scale proposed for X_a is tested against some of the existing studies including laboratory studies of Willis and Deardorff (1976, 1978), field experiments of Briggs (1993) and numerical models of Dosio et al. (2003); Weil et al. (2012); Nottrott et al. (2014) (Table 5). Willis and Deardorff (1976, 1978) conducted their experiments in a water tank with convective conditions of $w_* = 0.98\ cm/sec$ and $1.06\ cm/sec$; $\zeta \approx 40$ and released non-buoyant particles at $z_s/z_i = 0.067$ and 0.24 respectively. The CONDORS field experiment (Briggs, 1993) was conducted during late summer in a strongly convective atmosphere of $w_* = 1.81\ m/sec$ and $\zeta = 310$, during which tracer

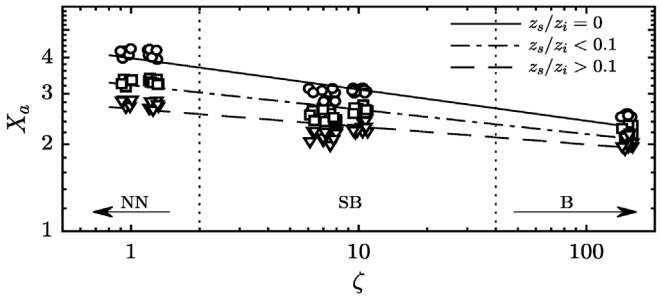

Fig. 9. Downwind distance at which mean plume height reaches asymptote vs stability parameter. Vertical dotted lines at $\zeta = 2$ and $\zeta = 40$ represents the break-down of three convective regimes used in the study. The straight line, dashed-dot line and dash-dash line represents the best-fit for data using power-law. The realizations for ground release are represented by circles, near surface release by squares and elevated release by downward-pointing triangles.

Table 5
Comparison of X_a from previous studies with the scaling proposed in Equation (8).

Study	z_s/z_i	ζ	Regime	X_a from study	X_a from Equ. (8)	%Difference
Willis and Deardorff (1976)	0.067	≈40	B	2.5	2.42	3.2
Willis and Deardorff (1978)	0.24	≈40	B	2	2.12	6
Briggs (1993)	0	310	B	2.25	2.17	3.6
	0.32	310	B	2	1.87	6.5
Dosio et al. (2003)	0.078	1.9	NN	3	3.09	3
	0.48	1.9	NN	2.3	2.56	6.7
	0.078	12.9	SB	2.9	2.65	8.6
	0.48	12.9	SB	2.5	2.28	8.8
Weil et al. (2012)	0	106	B	2.75	2.43	6.5
	0.32	106	B	2.2	2	9.1
Nottrott et al. (2014)	0.07	11	SB	2	2.02	1
	0.07	380	B	2.8	2.68	4.3

particles were released from $z_s/z_i = 0$ and 0.32. The numerical studies of Dosio et al. (2003) and Nottrott et al. (2014) consists of large-eddy scale modeling for dispersion of non-buoyant particles during weakly convective to strongly convective conditions with $\zeta = 1.9$ and 12.9 in Dosio et al. (2003); $\zeta = 11$ and 380 in Nottrott et al. (2014). Weil et al. (2012) used Lagrangian particle dispersion modeling to simulate the diffusion of particles in highly convective conditions with $w_* = 2\ m/sec$ and $\zeta = 106$. Our proposed scaling performed well with an average %difference of 5.6 between the observed X_a for all the studies considered and estimated X_a using equation (8). The maximum %difference of 9.1 occurred during the elevated release case of Weil et al. (2012).

Although plume dispersion tools and parameterizations exist that predict the short-term transport of passive elements in atmosphere, to authors knowledge, this is the first time, the plume transport is characterized in terms of atmospheric stability for a CBL using a high resolution numerical WRF with scalar transport model and using realistic initial and boundary conditions.

7. Summary

The dispersion of passive (non-buoyant and non-reactive) scalars in the convective atmospheric conditions is a complex phenomenon, which is dependent on the CBL dynamics. The short-term transport of plume dispersion under the CBL conditions is studied for Pure Convective, Shear-Buoyancy and Near-Neutral regimes. Mean plume characteristics are obtained from the ensemble properties of plume transport simulated during 12 days of winter and summer months covering the three different CBL regimes of interest. Meteorological conditions existing at the time of tracer release are observed to be key factors for accurate prediction of plume transport and dispersion. The initial mean wind speed at the release altitude for first 20–30 min after release, and the mean wind-speed at half the CBL depth at later times is suitable for short-term horizontal transport of the plume for surface and near-surface releases.

The numerical weather prediction model, WRF, fed with real boundary conditions serves as a robust tool for accurate prediction of mean plume behavior. WRF can model the large-scale atmospheric forcings that dictate the mean properties of passive scalars in convective conditions. WRF modeled atmospheric variables that govern the plume dynamics are found to be within the acceptable range of observations.

Conditions corresponding to high wind-shear and weak thermal forcings result in large horizontal transport scales, and with high plume concentration pockets advected close to their release altitude. The presence of thermal forcing influences the trajectory of plume centerline ($\overline{z}$) and also the vertical dispersion parameter (σ_z) along the downwind direction of the plume. The horizontal distance travelled by plume elements before they get well-mixed in CBL and growth rate of vertical dispersion parameter (σ_z/z_i), are highest for near-neutral, followed by combined shear- and buoyancy, and followed by pure convection regimes.

The asymptotic values of mean plume height and vertical dispersion as simulated by WRF during different convective conditions are with in the range of $0.5z_i - 0.53z_i$ and $0.4z_i - 0.55z_i$ respectively. For all the cases simulated, the mean plume height reaches an asymptote of approximately $0.5z_i$ suggesting that the plume elements are uniformly mixed in the CBL. The downwind distance at which this asymptote is reached depends on both convective strength and release altitude of the plume. The release height of the plume plays an important role for shear dominated convective conditions (NN regimes) compared to the buoyancy-dominated regimes. This is mainly due to the fact that the plume centerline asymptote is reached at a greater downwind distances. Whereas, for buoyancy dominated convective conditions (B regime), strong buoyancy forcing mixes the plume elements rapidly. The scaling law formulated for approximating the asymptote downwind distance based on release height and stability parameter is robust enough and performed well when compared with existing field, laboratory experiments and numerical models.

This study is unique from existing works in its implementation of WRF model for transport and dispersion of passive tracers at "grey-zone" resolutions ($100\ m < \Delta x < 1\ km$). Although, the framework presented in the current study uses actual geographical domain information and real boundary conditions, it is believed to yield satisfactory results for any location at a reasonable horizontal resolution and proper choice of physics and dynamics schemes used in WRF model set-up. Testing this set-up for different topographies, over complex terrains and various land usage categories is a promising scope for future work. The work is offered as a contribution to improved understanding of short-term plume transport in different convective regimes, and the transport scaling laws of the plume that depend on both the release height and also the CBL regime.

Conflict of interest

No conflict of interest.

Nomenclature

1. Monin-Obhukov length scale (L) (Monin and Obukhov, 1954)

$$L = \frac{-\rho_a c_p u_*^3 T}{\kappa g Q_0}$$

where, ρ_a, c_p, T are density, specific heat and surface temperature of

air, g is the gravitational constant, u_* is the friction velocity, κ is the von-Karman constant (typically $= 0.41$) and Q_0 is the surface kinematic heat flux.

2. Convective velocity

$$w_* = \left(\frac{g}{T_v} z_i \overline{w'\theta'_{v_s}}\right)^{1/3}$$

where, w_* is the Deardorff (or convective) velocity, T_v is the absolute virtual temperature, z_i is the depth of the convective boundary layer (CBL), $\overline{w'\theta'_{v_s}}$ is the kinematic heat flux at the surface.

3. Bulk-Richardson number

$$Ri_B = \frac{g\Delta\theta_v \Delta z}{\theta_v (\Delta \overline{U})^2}$$

where, θ_v is the virtual potential temperature, $\Delta\theta_v$ and $\Delta\overline{U}$ are the virtual potential temperature and mean wind speed differences across a layer of thickness Δz.

Acknowledgements

Funding for the present study is provided by U.S. Army Research Development and Engineering Command Edgewood Chemical Biological Center (ECBC) under grant # D01-W911SR-14-2-0001-0006. The authors gratefully thank colleagues at Laboratory of Turbulence and Intelligence Systems at UTSA for providing valuable suggestions and comments during the early stages of the manuscript. We are thankful to the WRF support team at NCAR for responding to our queries in a timely manner.

References

Avolio, E., Federico, S., Miglietta, M., Feudo, T.L., Calidonna, C., Sempreviva, A.M., 2017. Sensitivity analysis of wrf model pbl schemes in simulating boundary-layer variables in southern Italy: an experimental campaign. Atmos. Res. 192, 58–71.

Banta, R., Senff, C., Nielsen-Gammon, J., Darby, L., Ryerson, T., Alvarez, R., Sandberg, S., Williams, E., Trainer, M., 2005. A bad air day in houston. Bull. Am. Meteorol. Soc. 86 (5), 657–669.

Banta, R.M., Senff, C.J., White, A.B., Trainer, M., McNider, R.T., Valente, R.J., Mayor, S.D., Alvarez, R.J., Hardesty, R.M., Parrish, D., et al., 1998. Daytime buildup and nighttime transport of urban ozone in the boundary layer during a stagnation episode. J. Geophys. Res. Atmos. 103 (D17), 22519–22544.

Barr, S., Kyle, T.G., Clements, W.E., Sedlacek, W., 1983. Plume dispersion in a nocturnal drainage wind. Atmos. Environ. 17 (8), 1423–1429.

Bhaganagar, K., Bhimireddy, S.R., 2017. Assessment of the plume dispersion due to chemical attack on april 4, 2017, in Syria. Nat. Hazards 88 (3), 1893–1901.

Bierly, E.W., Hewson, E.W., 1962. Some restrictive meteorological conditions to be considered in the design of stacks. J. Appl. Meteorol. 1 (3), 383–390.

Blaylock, B.K., Horel, J.D., Crosman, E.T., 2017. Impact of lake breezes on summer ozone concentrations in the salt lake valley. J. Appl. Meteorol. Climatol. 56 (2), 353–370.

Briggs, G.A., 1965. A plume rise model compared with observations. J. Air Pollut. Control Assoc. 15 (9), 433–438.

Briggs, G.A., 1993. Plume dispersion in the convective boundary layer. part ii: analyses of condors field experiment data. J. Appl. Meteorol. 32 (8), 1388–1425.

Carvalho, D., Rocha, A., Gómez-Gesteira, M., Santos, C.S., 2014. Wrf wind simulation and wind energy production estimates forced by different reanalyses: comparison with observed data for Portugal. Appl. Energy 117, 116–126.

Coniglio, M.C., Correia Jr., J., Marsh, P.T., Kong, F., 2013. Verification of convection-allowing wrf model forecasts of the planetary boundary layer using sounding observations. Weather Forecast. 28 (3), 842–862.

Deardorff, J., 1970. Convective velocity and temperature scales for the unstable planetary boundary layer and for Rayleigh convection. J. Atmos. Sci. 27 (8), 1211–1213.

Deardorff, J., 1985. Laboratory experiments on diffusion:. the use of convective mixed-layer scaling. J. Clim. Appl. Meteorol. 24 (11), 1143–1151.

Dosio, A., Vilà-Guerau de Arellano, J., Holtslag, A.A., Builtjes, P.J., 2003. Dispersion of a passive tracer in buoyancy-and shear-driven boundary layers. J. Appl. Meteorol. 42 (8), 1116–1130.

Dudhia, J., 1989. Numerical study of convection observed during the winter monsoon experiment using a mesoscale two-dimensional model. J. Atmos. Sci. 46 (20), 3077–3107.

Ek, M., Mitchell, K., Lin, Y., Grunmann, P., Rogers, E., Gayno, G., Koren, V., Tarpley, J., 2003. Implementation of the upgraded noah land-surface model in the ncep operational mesoscale eta model. J. Geophys. Res. 108, 8851.

Ferber, G., Telegadas, K., Heffter, J., Dickson, C., Dietz, R., Krey, P., 1981. Demonstration of a Long-range Tracer System Using Perfluorocarbons. final report. Tech. rep., January, Tech. Report EPA-600.

Ferrier, B.S., Jin, Y., Lin, Y., Black, T., Rogers, E., DiMego, G., 2002. Implementation of a new grid-scale cloud and precipitation scheme in the ncep eta model. In: Conference on Weather Analysis and Forecasting, vol. 19. AMS, pp. 280–283.

Garratt, J., et al., 1992. The Atmospheric Boundary Layer, cambridge Atmospheric and Space Science Series. Camb. Univ. Press, Cambridge, pp. 416–444.

Gifford, F., 1960. Atmospheric dispersion calculations using the generalized Gaussian plume model. Nucl. Saf. 2 (2), 56–59.

Golder, D., 1972. Relations among stability parameters in the surface layer. Bound. Layer. Meteorol. 3 (1), 47–58.

Hong, S.-Y., Noh, Y., Dudhia, J., 2006. A new vertical diffusion package with an explicit treatment of entrainment processes. Mon. Weather Rev. 134 (9), 2318–2341.

Hu, X.-M., Nielsen-Gammon, J.W., Zhang, F., 2010. Evaluation of three planetary boundary layer schemes in the wrf model. J. Appl. Meteorol. Climatol. 49 (9), 1831–1844.

Janjic, Z., 1996. The surface layer parameterization in the ncep eta model. World Meteorol. Organ. Publ. WMO TD 4–16.

Kain, J.S., Fritsch, J.M., 1993. Convective parameterization for mesoscale models: the kain-fritsch scheme. In: The Representation of Cumulus Convection in Numerical Models. Springer, pp. 165–170.

Lyons, W.A., Cole, H.S., 1973. Fumigation and plume trapping on the shores of lake Michigan during stable onshore flow. J. Appl. Meteorol. 12 (3), 494–510.

Mlawer, E.J., Taubman, S.J., Brown, P.D., Iacono, M.J., Clough, S.A., 1997. Radiative transfer for inhomogeneous atmospheres: Rrtm, a validated correlated-k model for the longwave. J. Geophys. Res. Atmos. 102 (D14), 16663–16682.

Moeng, C.-H., Sullivan, P.P., 1994. A comparison of shear-and buoyancy-driven planetary boundary layer flows. J. Atmos. Sci. 51 (7), 999–1022.

Monin, A., Obukhov, A., 1954. Basic laws of turbulent mixing in the surface layer of the atmosphere. Contrib. Geophys. Inst. Acad. Sci. USSR 151 (163), e187.

Nieuwstadt, F., 1992. A large-eddy simulation of a line source in a convective atmospheric boundary layer I. dispersion characteristics. Atmos. Environ. Part A 26 (3), 485–495.

Noh, Y., Cheon, W., Hong, S., Raasch, S., 2003. Improvement of the k-profile model for the planetary boundary layer based on large eddy simulation data. Bound. Layer. Meteorol. 107 (2), 401–427.

Nottrott, A., Kleissl, J., Keeling, R., 2014. Modeling passive scalar dispersion in the atmospheric boundary layer with wrf large-eddy simulation. Atmos. Environ. 82, 172–182.

Petäjä, T., Järvi, L., Kerminen, V.-M., Ding, A., Sun, J., Nie, W., Kujansuu, J., Virkkula, A., Yang, X., Fu, C., et al., 2016. Enhanced air pollution via aerosol-boundary layer feedback in China. Sci. Rep. 6.

Schwartz, M., Elliott, D., 2006. Wind Shear Characteristics at central plains Tall Towers: Preprint. Tech. Rep. National Renewable Energy Laboratory (NREL), Golden, CO.

Skamarock, W.C., Klemp, J.B., 2008. A time-split nonhydrostatic atmospheric model for weather research and forecasting applications. J. Comput. Phys. 227 (7), 3465–3485.

Smith, K., Randall, G., Malcolm, D., Kelley, N., Smith, B., 2002. Evaluation of wind shear patterns at midwest wind energy facilities. In: WINDPOWER 2002 Conference. Am. Wind Energy Assoc. (AWEA).

Stull, R.B., 2012. An Introduction to Boundary Layer Meteorology, vol. 13 Springer Science & Business Media.

Sykes, R., Henn, D., 1989. Large-eddy simulation of turbulent sheared convection. J. Atmos. Sci. 46 (8), 1106–1118.

TCEQ, 2017. Texas commission on Environmental Quality. http://www17.tceq.texas.gov/tamis/index.cfm?fuseaction=report.site_list, Accessed date: September 2017.

Turner, D.B., 1994. Workbook of Atmospheric Dispersion Estimates: an Introduction to Dispersion Modeling. CRC Press.

Vanderwende, B., Lundquist, J.K., 2012. The modification of wind turbine performance by statistically distinct atmospheric regimes. Environ. Res. Lett. 7 (3), 034035.

Venkatram, A., 1984. The uncertainty in estimating dispersion in the convective boundary layer. Atmos. Environ. 18 (2), 307–310.

Weil, J.C., Sullivan, P.P., Patton, E.G., Moeng, C.-H., 2012. Statistical variability of dispersion in the convective boundary layer: ensembles of simulations and observations. Bound. Layer. Meteorol. 145 (1), 185–210.

Willis, G., Deardorff, J., 1976. A laboratory model of diffusion into the convective planetary boundary layer. Q. J. R. Meteorol. Soc. 102 (432), 427–445.

Willis, G., Deardorff, J., 1978. A laboratory study of dispersion from an elevated source within a modeled convective planetary boundary layer. Atmos. Environ. 12 (6–7), 1305–1311.

Yerramilli, A., Srinivas, C.V., Dasari, H.P., Tuluri, F., White, L.D., Baham, J., Young, J.H., Hughes, R., Patrick, C., Hardy, M.G., et al., 2009. Simulation of atmospheric dispersion of elevated releases from point sources in Mississippi gulf coast with different meteorological data. Int. J. Environ. Res. Public Health 6 (3), 1055–1074.

Yu, S., Mathur, R., Pleim, J., Pouliot, G., Wong, D., Eder, B., Schere, K., Gilliam, R., Rao, S.T., 2012. Comparative evaluation of the impact of wrf-nmm and wrf-arw meteorology on cmaq simulations for o3 and related species during the 2006 texaqs/go-maccs campaign. Atmos. Pollut. Res. 3 (2), 149–162.

Yver, C., Graven, H., Lucas, D.D., Cameron-Smith, P., Keeling, R., Weiss, R., 2013. Evaluating transport in the wrf model along the California coast. Atmos. Chem. Phy. 13 (4), 1837–1852.